

星形成ゼミ 2023/11/17 #369 15-28 辰馬 (理研数理創造プログラム)

- 15. FAUST X: Formaldehyde in the Protobinary System [BHB2007] 11: Small Scale Deuteration
- 16. Evolution of Chemistry in the envelope of Hot Corinos (ECHOS). I. Extremely young sulphur chemistry in the isolated Class 0 object B335
- 17. Millimetre and submillimetre spectroscopy of isobutene and its detection in the molecular cloud G+0.693
- 18. Millimeter emission in photoevaporating disks is determined by early substructures**
- 19. A global view on star formation: The GLOSTAR Galactic plane survey VIII. Formaldehyde absorption in Cygnus X
- 20. Protonated hydrogen cyanide as a tracer of pristine molecular gas
- 21. JOYS: Disentangling the warm and cold material in the high-mass IRAS 23385+6053 cluster
- 22. Grain Growth and Dust Segregation Revealed by Multi-wavelength Analysis of the Class I Protostellar Disk WL 17**
- 23. Delivery of icy planetesimals to inner planets in the Proxima Centauri planetary system
- 24. The Global Structure of Molecular Clouds: I. Trends with Mass and Star Formation Rate
- 25. The population of young low-mass stars in Trumpler 14
- 26. Rotational Variability and Detection of Superflares in a Young Brown Dwarf by TESS
- 27. SOFIA FEEDBACK Survey: The Pillars of Creation in [C II] and Molecular Lines
- 28. A resolved rotating disk wind from a young T Tauri star in the Bok globule CB26

Grain Growth and Dust Segregation Revealed by Multi-wavelength Analysis of the Class I Protostellar Disk WL 17

Ilseung Han, Woojin Kwon, Yusuke Aso, Jaehan Bae, Patrick Sheehan ★ The first step toward planet formation is grain growth from (sub-)micrometer to millimeter/centimeter sizes. Grain growth has been reported not only in Class II protoplanetary disks but also in Class 0/I protostellar envelopes. However, early-stage grain growth occurring in Class 0/I stages has rarely been observed on the protostellar disk scale. Here we present the results from the ALMA Band 3 ($\lambda = 3.1$ mm) and 7 ($\lambda = 0.87$ mm) archival data of the Class I protostellar disk WL 17 in the ρ Ophiuchus molecular cloud. Disk substructures are found in both bands, but they are different: while a central hole and a symmetric ring appear in Band 3, an off-center hole and an asymmetric ring are shown in Band 7. Furthermore, we obtain an asymmetric spectral index map with a low mean value of $\alpha = 2.28 \pm 0.02$, suggestive of grain growth and dust segregation on the protostellar disk scale. Our radiative transfer modeling verifies these two features by demonstrating that 10 cm-sized large grains are symmetrically distributed, whereas 10 μm -sized small grains are asymmetrically distributed. Also, the analysis shows that the disk is expected to be massive and gravitationally unstable. We thus suggest a single Jupiter-mass protoplanet formed by gravitational instability as the origin of the ring-like structure, grain growth, and dust segregation identified in WL 17.

Grain Growth and Dust Segregation Revealed by Multi-wavelength Analysis of the Class I Protostellar Disk WL 17 (Han et al. 2023)

アブストラクト

- 目的: Class 0/Iの原始星エンベロープでのダスト成長を調べた。
- 方法: ρ Ophiuchus分子雲中のClass I原始星円盤WL 17の3.1, 0.87 mmのALMAアーカイブデータを解析した。
- 結果: 円盤のsubstructuresが、3.1 mmでは対称リングと中心の穴だが、0.87 mmでは非対称リングと中心のズレた穴であることがわかった。スペクトル指数の平均値は $\alpha = 2.28 \pm 0.02$ で、ダスト成長と原始星円盤スケールでのダストのサイズ分別が起きていることがわかった。
- 結論: 10 cmのダストが対称的に分布し、10 μm のダストは非対称に分布していると考えられる。また、円盤は重く重力的に不安定であると示唆される。すなわちWL 17のリング状構造やダスト成長、ダスト分別の起源としては、重力不安定で形成された1つの木星質量の原始惑星が考えられる。

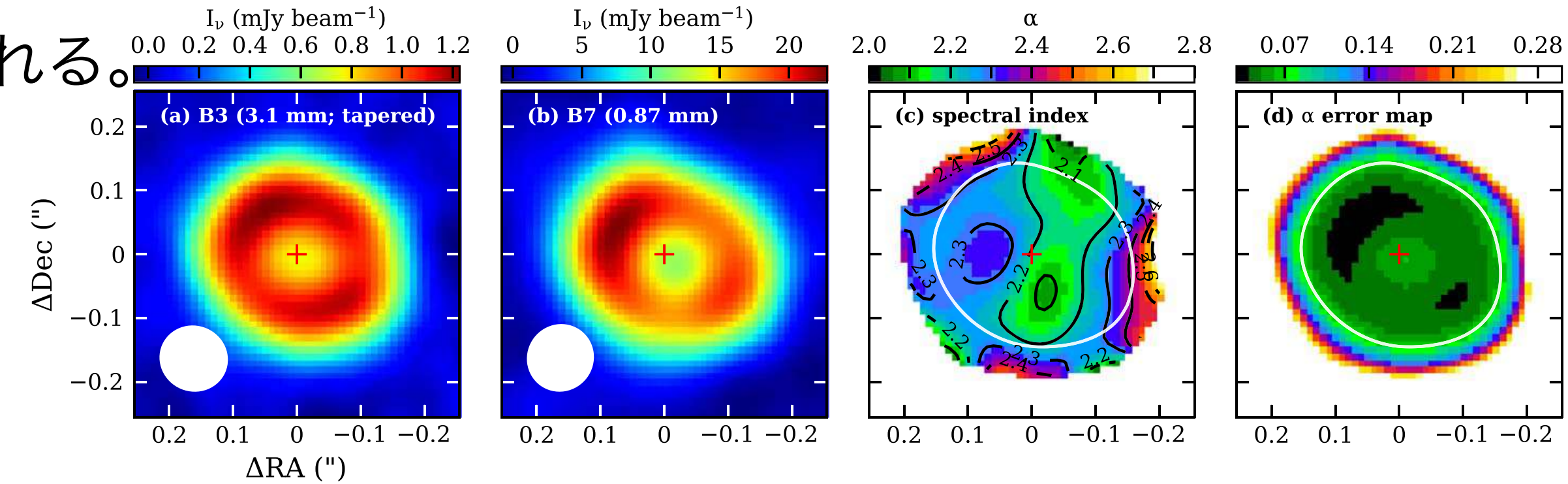


Figure 2. ALMA images of WL 17. (a) Tapered Band 3 dust continuum image with the synthesized beam of $0''.108 \times 0''.103$ (PA = 67°) with the sensitivity of $34 \mu\text{Jy beam}^{-1}$. The red plus sign indicates the position of the protostar. The original Band 3 image is shown in Figure 1. (b) Band 7 dust continuum image with the synthesized beam of $0''.107 \times 0''.104$ (PA = 67°) with the sensitivity of $0.4 \text{ mJy beam}^{-1}$. Note that substructures are different between Bands 3 and 7. (c) Spectral index (α) map between Bands 3 and 7. The α values are overall small with a mean value of 2.28 ± 0.02 , and also they are distributed asymmetrically. (d) Statistical error map of spectral indices. The white contours of panels (c) and (d) mark where the error level is 0.07.

Grain Growth and Dust Segregation Revealed by Multi-wavelength Analysis of the Class I Protostellar Disk WL 17 (Han et al. 2023)

背景

- ダストサイズは(サブ)ミリ波のダストオパシティスペクトル指数 β で見積もることができる。
光学的に薄いという仮定と、Rayleigh–Jean’s近似を用いると、スペクトル指数 α との関係は $\alpha = \beta + 2$ である。
(次のページで詳しく説明)
- 1 mm波長で $\beta \leq 1.0$ の場合、ダストサイズは3 mmよりも大きい(Draine 2006)
- サブミクロンサイズの星間空間ダストは $\beta \approx 1.7$

この論文でやったこと

- ALMA Band 3, 7のアーカイブデータを用いて、
Class I原始星円盤WL 17を解析し、ダストサイズや分布を調べた。
WL17: M3型原始星、 ≤ 0.7 Myrのlate Class I原始星
円盤: Band 3の高空間分解能観測によると、
12 auの中心の穴、horseshoe-likeな狭いリング(幅11 au, 位置23 au)

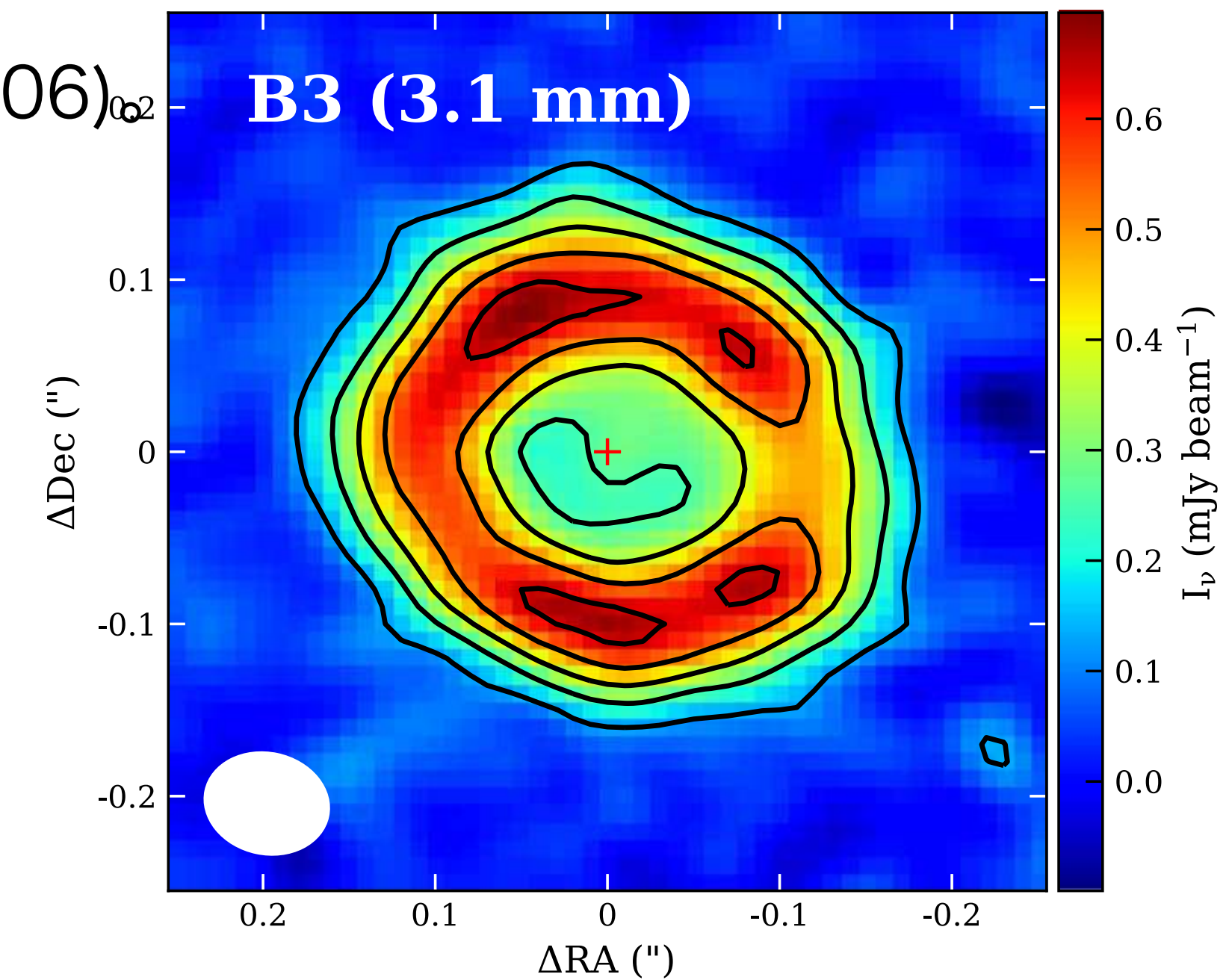


Figure 1. ALMA Band 3 (3.1 mm; 97.5 GHz) continuum image of the Class I protostellar disk WL 17. Contour levels are $\{4, 8, 12, 16, 20\} \times \sigma_{B3}$, where σ_{B3} corresponds to $33 \mu\text{Jy beam}^{-1}$. Particularly, the noncircular $8\sigma_{B3}$ contour implies the weak emission in the central hole, which was previously reported in Sheehan & Eisner (2017). The synthesized beam size shown at the lower left is $0''.074 \times 0''.060$ with $\text{PA} = 74^\circ$. The red plus sign indicates the position of the protostar.

Grain Growth and Dust Segregation Revealed by Multi-wavelength Analysis of the Class I Protostellar Disk WL 17 (Han et al. 2023)

結果

- ダスト質量: $M_{\text{dust}} = \frac{F_{\nu} d^2}{\kappa_{\nu} B_{\nu}(T_{\text{dust}})}$, $\kappa_{\nu} = 10 (\nu/1 \text{ THz})^{\beta}$: ダスト質量吸収係数(ダストオパシティ)
30 Kとすると、Band 3では26 M_{earth}、Band 7では13 M_{earth}。
ダスト質量の違いはダストオパシティの推定($\beta = 1$ を仮定)による → 質量を同じにするには $\beta < 1$ の必要がある
→ (サブ)ミリ波で $\beta < 1$ は、mm-cmサイズのダストが光学的に薄い円盤赤道面に存在していることを示唆する。
→ ダストが成長している。
- ダストオパシティスペクトル指数 β ($\kappa_{\nu} \propto \nu^{\beta}$, の β) はダストサイズ、形状、組成、porosityに依存する。
→ ダスト成長を調べるために使われている。
- スペクトル指数: $\alpha = \log(I_{\nu_1}/I_{\nu_2})/\log(\nu_1/\nu_2)$,
$$\alpha = 3 - \frac{h\nu}{k_B T_{\text{dust}}} \frac{e^{h\nu/k_B T_{\text{dust}}}}{e^{h\nu/k_B T_{\text{dust}}} - 1} + \frac{\tau_{\nu}}{e^{\tau_{\nu}} - 1} \beta,$$

光学的に薄い場合($\tau_{\nu} \ll 1$)、Rayleigh-Jeans近似が使えて、 $\alpha = \beta + 2$ となる。
光学的に厚い場合($\tau_{\nu} \gg 1$)でRayleigh-Jeans近似の場合は、 $\alpha = 2$ となり、 β が関係なくなる。
→ α から β を求めるためには、光学的厚さを測定することが必要。

Grain Growth and Dust Segregation Revealed by Multi-wavelength Analysis of the Class I Protostellar Disk WL 17 (Han et al. 2023)

結果

- プランク関数を用いた光学的厚さの計算 → 平均値がBand 3で0.35、Band 7で0.57 → $\alpha = 1.84 + 0.79\beta$.

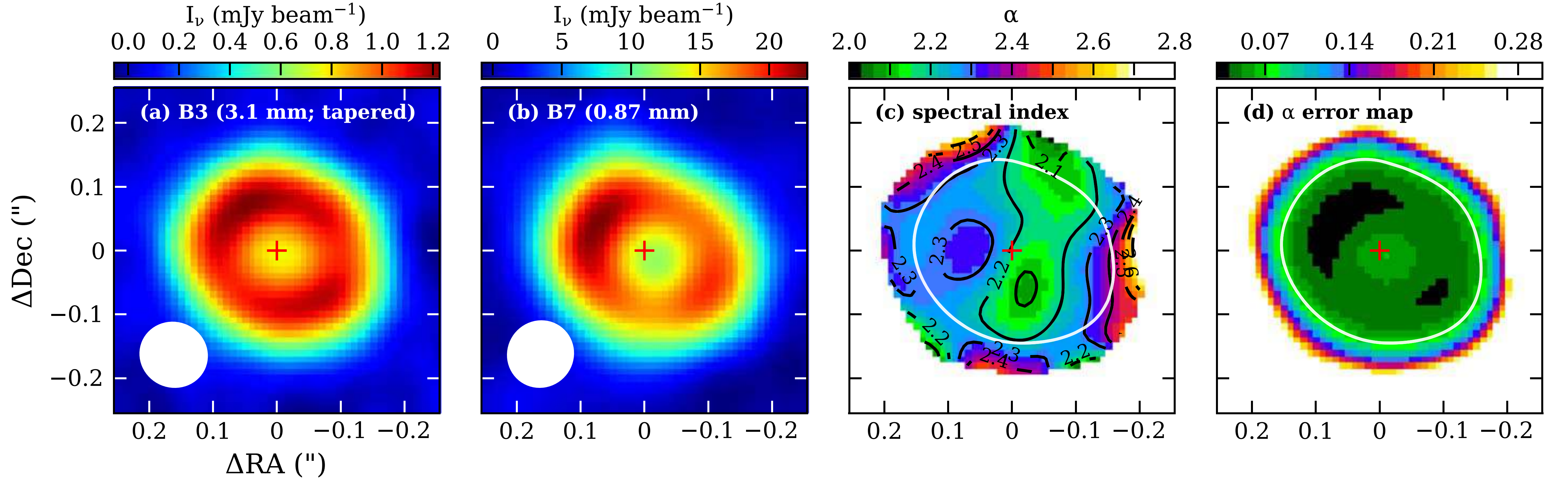


Figure 2. ALMA images of WL 17. (a) Tapered Band 3 dust continuum image with the synthesized beam of $0''.108 \times 0''.103$ (PA = 67°) with the sensitivity of $34 \mu\text{Jy beam}^{-1}$. The red plus sign indicates the position of the protostar. The original Band 3 image is shown in Figure 1. (b) Band 7 dust continuum image with the synthesized beam of $0''.107 \times 0''.104$ (PA = 67°) with the sensitivity of $0.4 \text{ mJy beam}^{-1}$. Note that substructures are different between Bands 3 and 7. (c) Spectral index (α) map between Bands 3 and 7. The α values are overall small with a mean value of 2.28 ± 0.02 , and also they are distributed asymmetrically. (d) Statistical error map of spectral indices. The white contours of panels (c) and (d) mark where the error level is 0.07.

Grain Growth and Dust Segregation Revealed by Multi-wavelength Analysis of the Class I Protostellar Disk WL 17 (Han et al. 2023)

結果

- $\beta = 0.56 \pm 0.03 \rightarrow$ ダストサイズ分布が $n(a) \propto a^{-q}$, とすると、 $a_{\max} = 0.2\text{--}20\text{ cm}$ and $q = 2.5\text{--}3.0$.
 \rightarrow late Class I 原始星 ($\leq 0.7\text{ Myr}$) ですでに cm サイズまでダストが成長している。
(他にそのような Class I は EC 53; Lee+2020b, CB 26; Zhang+2021 とか)
- α が非対称に分布している \rightarrow ダストがサイズによって異なる分布をしている。

輻射輸送モデル(RADMC-3D; Dullemond+2012)

- ダストオパシティ: DIANA (Disc ANALysis project; Woitke+2016)
 $n(a) \propto a^{-q}$ from $a_{\min} = 0.05\text{ }\mu\text{m}$
 $a_{\max} = \{10\text{ }\mu\text{m}, 100\text{ }\mu\text{m}, 1\text{ mm}, 1\text{ cm}, 10\text{ cm}\}$, $q = \{2.5, 3.0, 3.5\}$
- 観測に合うパラメータを探した: \uparrow 以外は (Σ_{hole} , Σ_{ring} , R_{ring} , and σ_{ring})

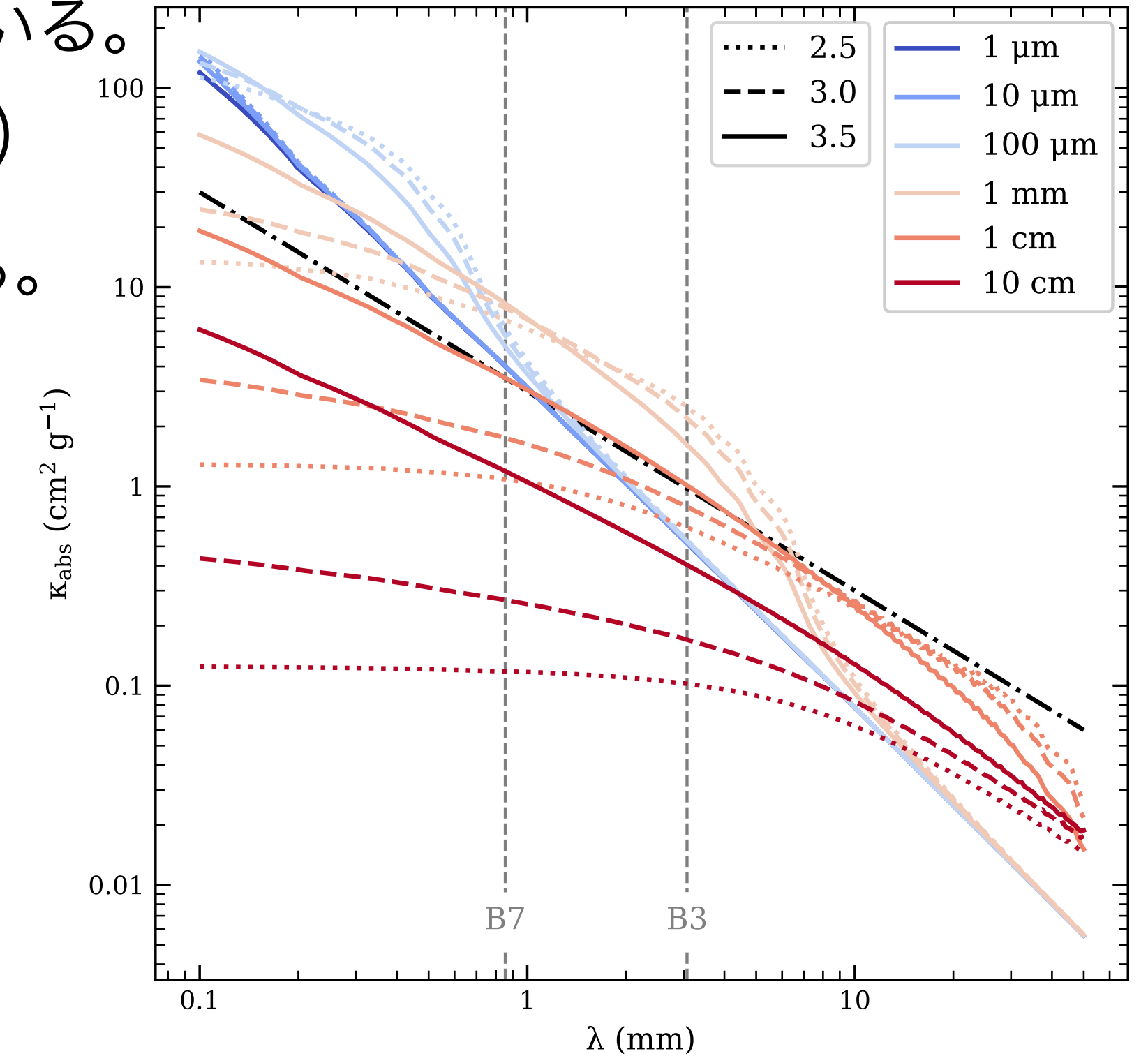


Figure 3. DIANA dust absorption opacities used for radiative transfer modeling. The 15 adopted opacities and $a_{\max} = 1\text{ }\mu\text{m}$ opacities have different line colors and styles depending on a_{\max} and q . Two gray dashed vertical lines correspond to ALMA Band 3 (3.1 mm) and 7 (0.87 mm) wavelengths. For comparison, the opacity computed in Beckwith et al. (1990) is indicated by a black dashed-dotted line. Note that this widely used opacity is particularly similar to the DIANA opacity with $a_{\max} = 1\text{ cm}$ and $q = 3.5$.

Grain Growth and Dust Segregation Revealed by Multi-wavelength Analysis of the Class I Protostellar Disk WL 17 (Han et al. 2023)

モデルとの比較結果

- Band 3とBand 7をよく説明できたのは、
(a_{\max} , q) = (1 cm, 2.5), (10 cm, 2.5), (10 cm, 3.0)
特にBand 7の中心の穴の再現が難しかった。
- Band 7は完璧には説明できず、ミクロンサイズのダストが非対称に分布しているのではないかとと思われる。
ロスビー波不安定による渦？

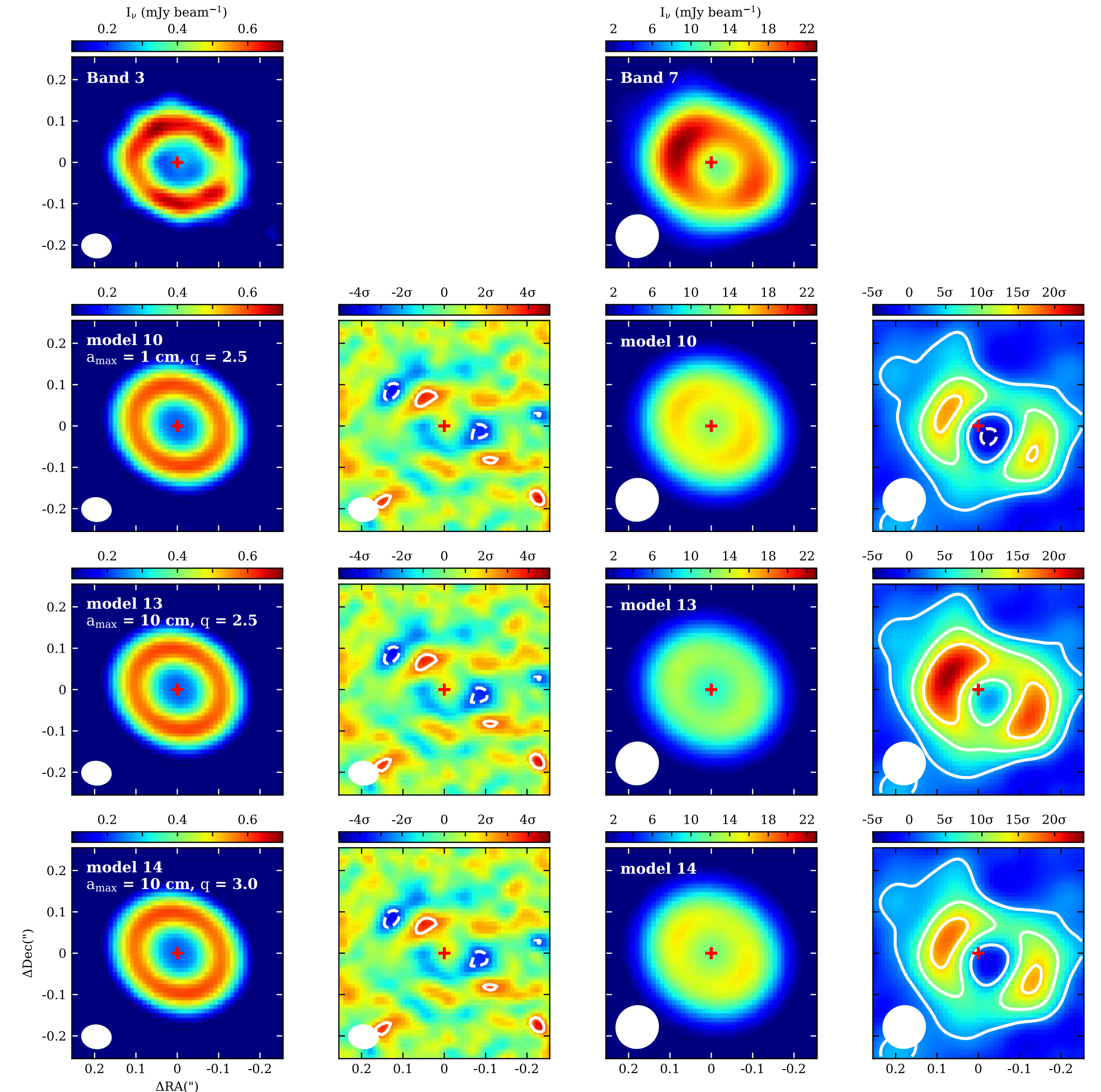


Figure 4. Part of the 15 best-fit models depending on a_{\max} and q . The top two panels are the same as the Band 3 and 7 data shown in Figures 1 and 2(b). The red star indicates the position of the protostar. The remaining panels are the model images. From the left, the first column shows the three Band 3 model images depending on a_{\max} and q , the second column shows their residual maps obtained by subtracting individual models from the Band 3 observational image, the third column shows the Band 7 model images, and the fourth column shows their residual maps obtained by subtracting individual models from the Band 7 observational image. Contour levels in the Band 3 and 7 residual maps are $\{-3, 3\}$, where $\sigma_{B3} = 33 \mu\text{Jy beam}^{-1}$, and $\{-3, 3, 9, 15\}$, where $\sigma_{B7} = 0.4 \text{ mJy beam}^{-1}$, respectively. Note that only these three models, mainly populated by centimeter-sized large grains, reproduce well the central hole in Band 7.

Grain Growth and Dust Segregation Revealed by Multi-wavelength Analysis of the Class I Protostellar Disk WL 17 (Han et al. 2023)

議論

- WL 17の円盤の構造が惑星起源である可能性が高い。

Kanagawa+2016を用いた惑星質量推定: $0.9 M_J$

→ 重力不安定で早く形成された？

→ Toomre Q を計算: $Q = \frac{c_s \Omega}{\pi G \Sigma}$

- Toomre Q

重力不安定条件: $Q_{\min} \lesssim 0.9 - 1.5$

→ リングで不安定になっている。

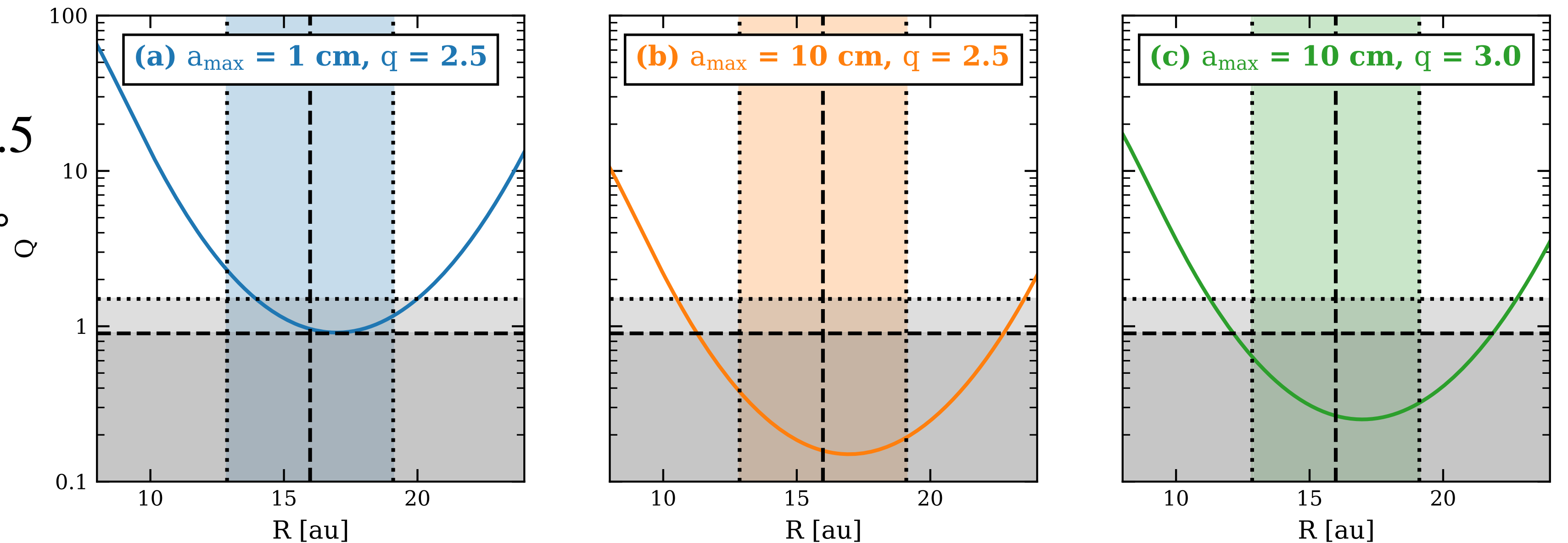


Figure 7. Toomre Q parameter radial profiles of three best-fit models with (a) $a_{\max} = 1$ cm and $q = 2.5$, (b) $a_{\max} = 10$ cm and $q = 3.0$, and (c) $a_{\max} = 10$ cm and $q = 3.0$. To focus on GI in the ring region, these profiles show between 8 and 24 au. In the vertical direction, the black dashed and dotted lines indicate $R_{\text{hole}} \simeq 16.0$ au and $\sigma_{\text{ring}} \simeq 3.1$ au of the best-fit models, respectively, and the ring region is shown as the shaded region in each panel. In the horizontal direction, the black dashed and dotted lines indicate the critical Toomre Q parameter values of 0.9 (Backus & Quinn 2016) and 1.5 (Boss 2006), respectively, for a protostellar disk around an M-type protostar with $1 M_{\odot}$. The gray shaded regions below these two lines are gravitationally unstable, meaning that Jupiter-mass planet(s) can rapidly form within the ring region.

Millimeter emission in photoevaporating disks is determined by early substructures

Matías Gárate, Til Birnstiel, Paola Pinilla, Sean M. Andrews, Raphael Franz, Sebastian Markus Stammer, Giovanni Picogna, Barbara Ercolano, Anna Miotello, Nicolás T. Kurtovic ★ [abridged]

Photoevaporation and dust-trapping are individually considered to be important mechanisms in the evolution and morphology of protoplanetary disks. We studied how the presence of early substructures affects the evolution of the dust distribution and flux in the millimeter continuum of disks that are undergoing photoevaporative dispersal. We also tested if the predicted properties resemble those observed in the population of transition disks. We used the numerical code Dustpy to simulate disk evolution considering gas accretion, dust growth, dust-trapping at substructures, and mass loss due to X-ray and EUV (XEUV) photoevaporation and dust entrainment. Then, we compared how the dust mass and millimeter flux evolve for different disk models. We find that, during photoevaporative dispersal, disks with primordial substructures retain more dust and are brighter in the millimeter continuum than disks without early substructures, regardless of the photoevaporative cavity size. Once the photoevaporative cavity opens, the estimated fluxes for the disk models that are initially structured are comparable to those found in the bright transition disk population ($F_{\text{mm}} > 30 \text{ mJy}$), while the disk models that are initially smooth have fluxes comparable to the transition disks from the faint population ($F_{\text{mm}} < 30 \text{ mJy}$), suggesting a link between each model and population. Our models indicate that the efficiency of the dust trapping determines the millimeter flux of the disk, while the gas loss due to photoevaporation controls the formation and expansion of a cavity, decoupling the mechanisms responsible for each feature. In consequence, even a planet with a mass comparable to Saturn could trap enough dust to reproduce the millimeter emission of a bright transition disk, while its cavity size is independently driven by photoevaporative dispersal.

Millimeter emission in photoevaporating disks is determined by early substructures (Gárate et al. 2023)

アブストラクト

- 目的: 原始惑星系円盤のギャップなどのsubstructuresのありなしが、光蒸発による散逸を受けている円盤のダスト分布やミリ波連続波のフラックスに与える影響を調べた。さらに、遷移円盤の観測との比較も行った。
- 方法: Dustpyを用いて、ガス降着・ダスト成長・substructuresによるダスト捕獲・X線とEUVによる光蒸発を考慮した計算を行い、円盤進化を調べた。異なる円盤モデルで、ダスト質量やミリ波フラックスの進化を比較した。
- 結果: 光蒸発による散逸の間、光蒸発によるcavityの大きさに関わらず、substructuresのある円盤のほうがより多くのダストを保持し、ミリ波連続波で明るくなることがわかった。光蒸発によるcavityが開くと、substructuresのある円盤のフラックスは明るい遷移円盤($F_{\text{mm}} > 30 \text{ mJy}$)に匹敵し、なめらかな円盤のフラックスは暗い遷移円盤($F_{\text{mm}} < 30 \text{ mJy}$)に匹敵することがわかった。
- 結論: ダスト捕獲の効率が円盤のミリ波フラックスを決める一方、光蒸発によるガス損失がcavity形成や成長を決め、それぞれのメカニズムは分離している。その結果、土星質量くらいの(そんなに重くないという意味)惑星ですら、明るい遷移円盤のミリ波放射を再現するダストを十分に捕獲できる。一方、cavityの大きさは光蒸発散逸により独立的に決まる。

Millimeter emission in photoevaporating disks is determined by early substructures (Gárate et al. 2023)

背景

- 円盤寿命よりも早い円盤散逸が観測より示唆されている。
- 遷移円盤を説明するものとして、光蒸発が提案されている。
光蒸発とは: 高エネルギーの光子(Far UV, Extreme UV, X-ray)が円盤表面のガス粒子にぶつかり、中心星の重力ポテンシャルから解放させる現象。
遷移円盤のSEDの近赤外や中間赤外の欠損 → 内側領域での小さな粒子の欠乏 → 光蒸発によるcavityと一致
- 遷移円盤はミリ波フラックスの観点から2種類に分けられている。 $F_{\text{mm}} = 30 \text{ mJy} \cdot (d/140 \text{ pc})^{-2}$

この論文でやったこと

- 1次元モデルを用いたダストダイナミクスの観点から、光蒸発円盤の進化を調べた。
ダスト成長・破壊(Brinstiel+2010)、X-rayとEUVの光蒸発モデル(Picogna+2019)、光蒸発風によるダスト粒子の損失(Franz+2020)
- 観測とも比較した。

Millimeter emission in photoevaporating disks is determined by early substructures (Gárate et al. 2023)

円盤モデル

- ガス進化: 粘性拡散と光蒸発による質量損失。ギャップあり (Gaussian bump)。中心星による加熱で温度が決まる。

$$\frac{\partial}{\partial t} \Sigma_g = \frac{3}{r} \frac{\partial}{\partial r} \left(r^{1/2} \frac{\partial}{\partial r} (\nu \Sigma_g r^{1/2}) \right) - \dot{\Sigma}_w,$$

- ダスト進化 (Brinstiel+2010): 移流、拡散、凝集、破壊。

$$\frac{\partial}{\partial t} (r \Sigma_d) + \frac{\partial}{\partial r} (r \Sigma_d v_d) - \frac{\partial}{\partial r} \left(r D_d \Sigma_g \frac{\partial}{\partial r} \epsilon \right) = -\dot{\Sigma}_{w,d},$$

- 光蒸発モデル:

$$\dot{\Sigma}_{w,d} = \epsilon_w \dot{\Sigma}_w,$$

$$\epsilon_w(a) = \frac{\int_{h_w}^{\infty} \rho_d(z, a) dz}{\int_{h_w}^{\infty} \rho_g(z) dz},$$

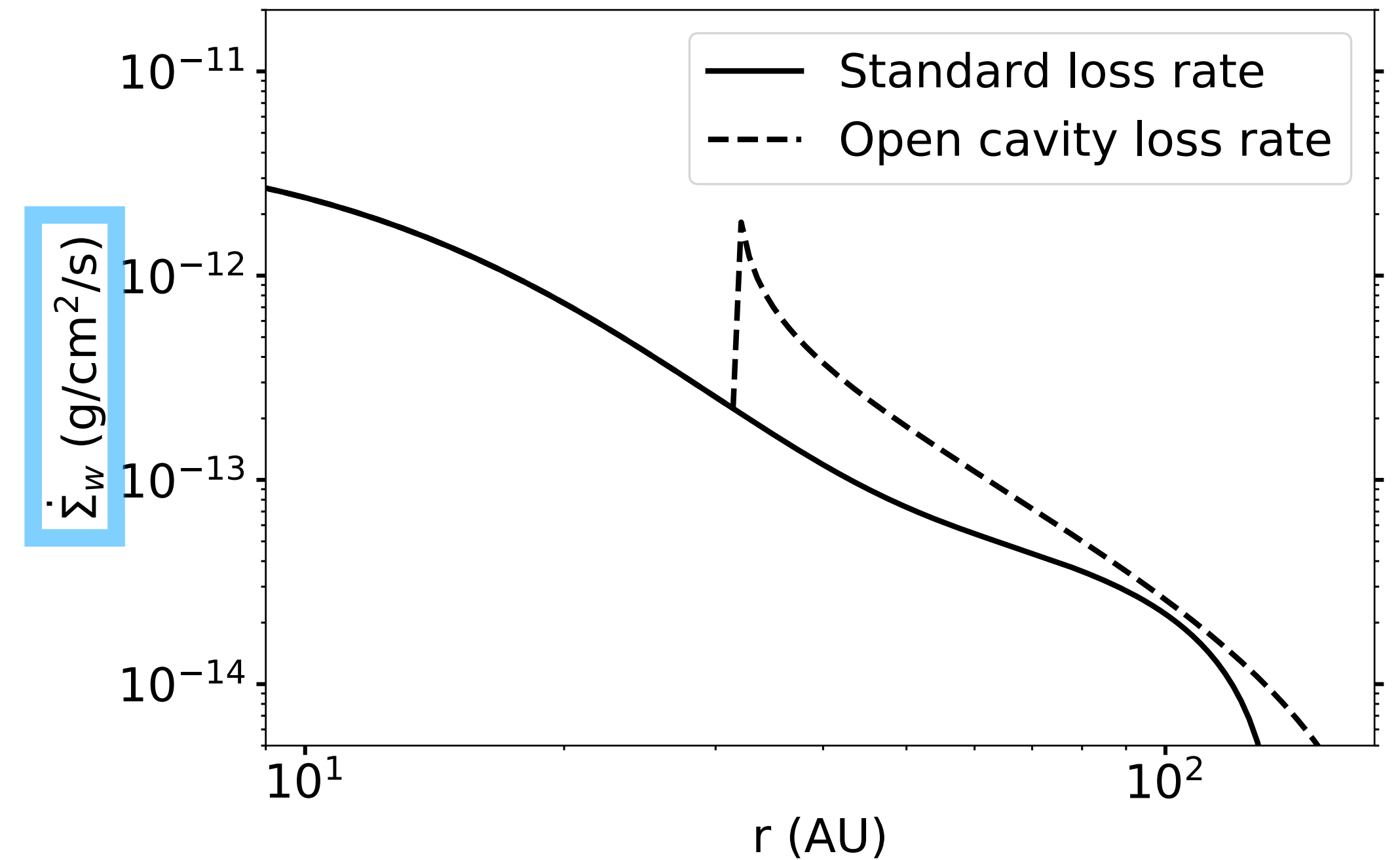


Fig. 1. Example of the gas loss rate profile, following the photoevaporation model from Picogna et al. (2019, their Equations 2 and 4), for $L_x = 10^{30} \text{ erg s}^{-1}$. The figure shows the mass loss rate before the photoevaporative cavity opens (solid line) and after the photoevaporative cavity opens (dashed line), with the cavity edge located at $r_{\text{cavity}} \approx 30 \text{ AU}$ after 1.9 Myr of evolution.

Millimeter emission in photoevaporating disks is determined by early substructures (Gárate et al. 2023)

シミュレーション設定(DustPy)

- 初期設定
中心星: 0.7 M_sun, 1.7 R_sun, 4500 K
初期ダストガス比: $\epsilon_0 = 1.5 \times 10^{-2}$, 初期ダスト最大サイズ: 1 μm
コンパクトダスト、表面はice、物質密度: $\rho_s = 1.6 \text{ g cm}^{-3}$ (silicate core?), 破壊速度: $v_{\text{frag}} = 10 \text{ m s}^{-1}$
計算領域: 4–300 au、計算ダストサイズ: 0.5 μm –20 cm
光蒸発風 → 1+1D (各動径方向のグリッドで鉛直方向のグリッドを考え、ダストガス損失比を計算する) < 10 h_g
- 1.3 mmでのフラックスの求め方: vertical slab近似 or 輻射輸送計算
vertical slab近似: 自己散乱を無視している。光蒸発のcavityの端で温度構造が照射円盤とは一致しなくなる。
輻射輸送計算: RADMC-3D (Dullemond+2012)でダスト温度、1.3 mmフラックス、0.1 μm –1 cmのSEDを計算。
opacity: DSHARP (Birnstiel+2018): 水氷、FeS、耐火性有機物、astronomical silicateの組成を持つコンパクトダスト粒子。OpTool (Dominik+2021)でコンパクト粒子のミー散乱を用いてopacityを求める。

● パラメータ	<div></div>	
	Variable	Value
	L_x [$10^{30} \text{ erg s}^{-1}$]	0.3, 1.0 , 3.0 ← x-ray
	r_{gap} [AU]	20, 40 , 60
	A_{gap}	0 , 1, 2, 4 ← 0はギャップなし

光蒸発風で損失するダストは $\leq 10 \mu\text{m}$ 、 $\geq 3 \text{ h}_g$

Millimeter emission in photoevaporating disks is determined by early substructures (Gárate et al. 2023)

結果

- substructuresがあるとダストが残りやすい。
初期 ~ 200 M_{earth}
→ 1 Myr後に77 M_{earth} (構造あり)、4 M_{earth} (なし)
- 光蒸発によるcavityが空いたあとのダスト質量の減少は、
構造のある円盤: 77→55 M_{earth}
構造のない円盤: 4→3 M_{earth}
cavityが開くと光蒸発によるダスト損失率は大きくなるが、
ダスト損失はほとんど円盤進化初期に起こっている。

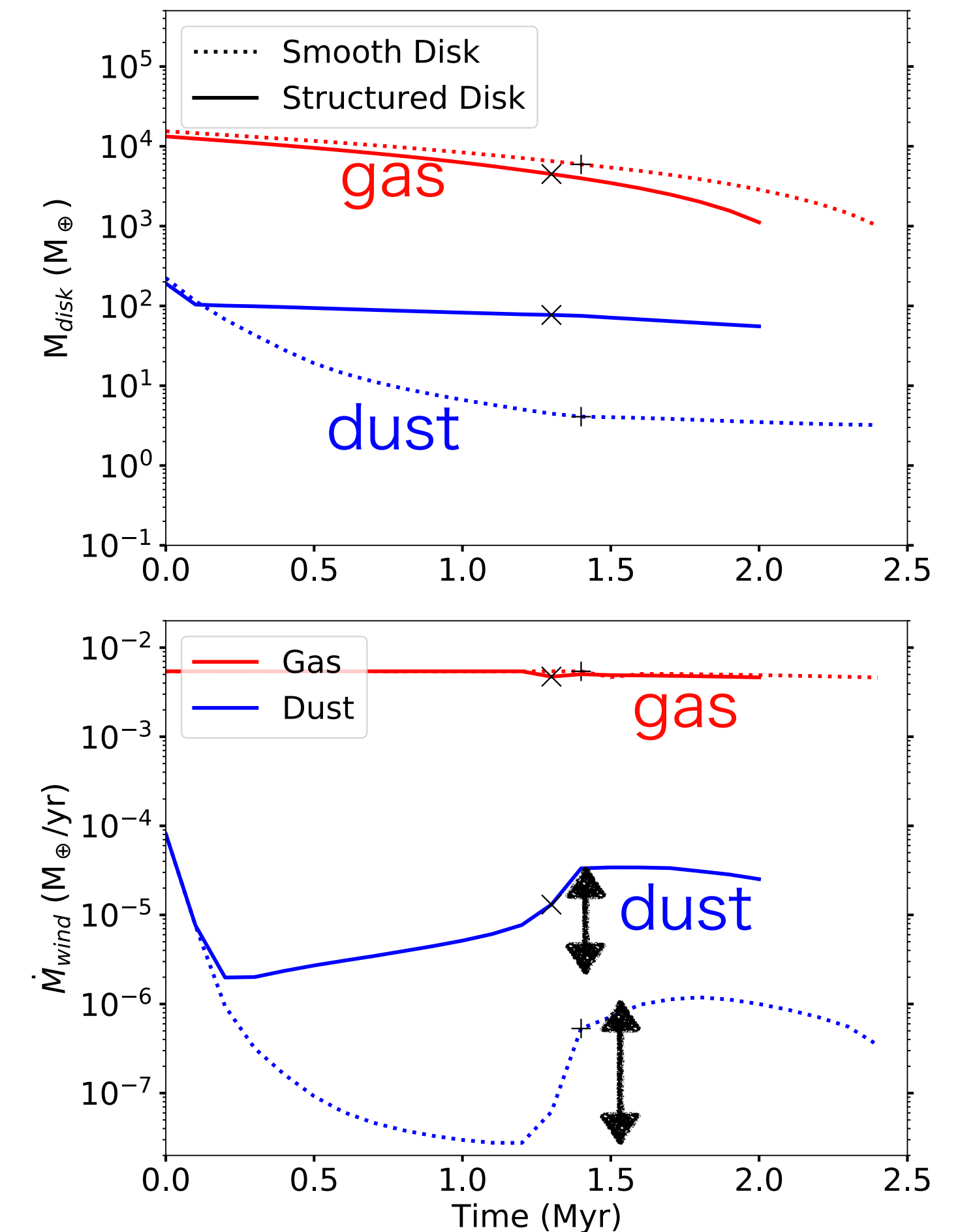


Fig. 2. *Top:* Mass evolution of the disk mass in gas (red lines) and dust (blue lines). *Bottom:* Evolution of the mass loss rate of gas and dust by photoevaporative winds. The markers indicate the moment when photoevaporation opens a cavity in the inner disk (“+” for the initially smooth disk, “x” for the initially structured disk).

Millimeter emission in photoevaporating disks is determined by early substructures (Gárate et al. 2023)

結果

- 構造なし: 光蒸発による穴の外側でダストがたまり、1つのリングになる。
- 構造あり: 元のリングと光蒸発によるリングの2つができ、後に1つに合体する。

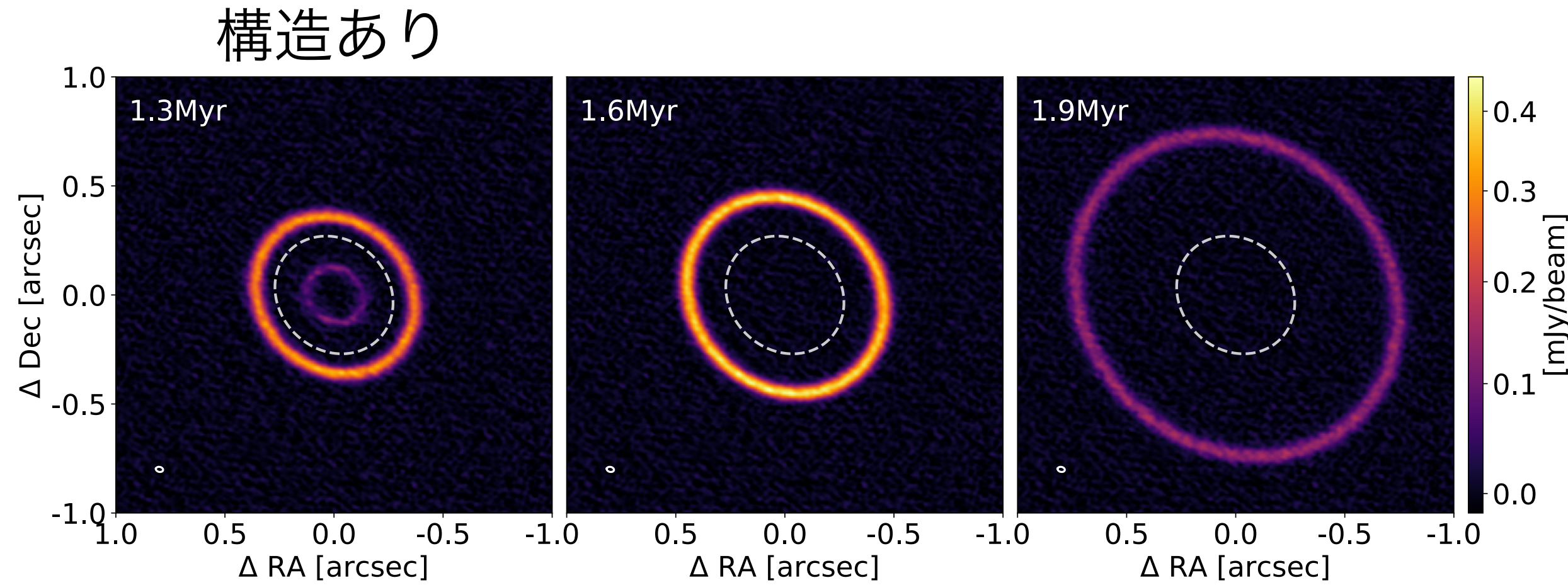


Fig. 11. Synthetic ALMA observations at 1.3 mm of the structured disk model at 1.3 Myr, 1.6 Myr, and 1.8 Myr, generated using the SIMIO package (Kurtovic et al., in prep.) to post-process our radiative transfer model. The image shows how our disk would look if it was observed with the same ALMA configuration of Elias24 (Huang et al. 2018, from the DSHARP sample), assuming a distance of 139 pc and an inclination of 29°. The beam size is plotted in the lower-left corner. The orbit of the primordial gap ($r_{\text{gap}} = 40$ AU) is marked with a dashed line. We note that this is not intended to be a comparison “with” Elias24.

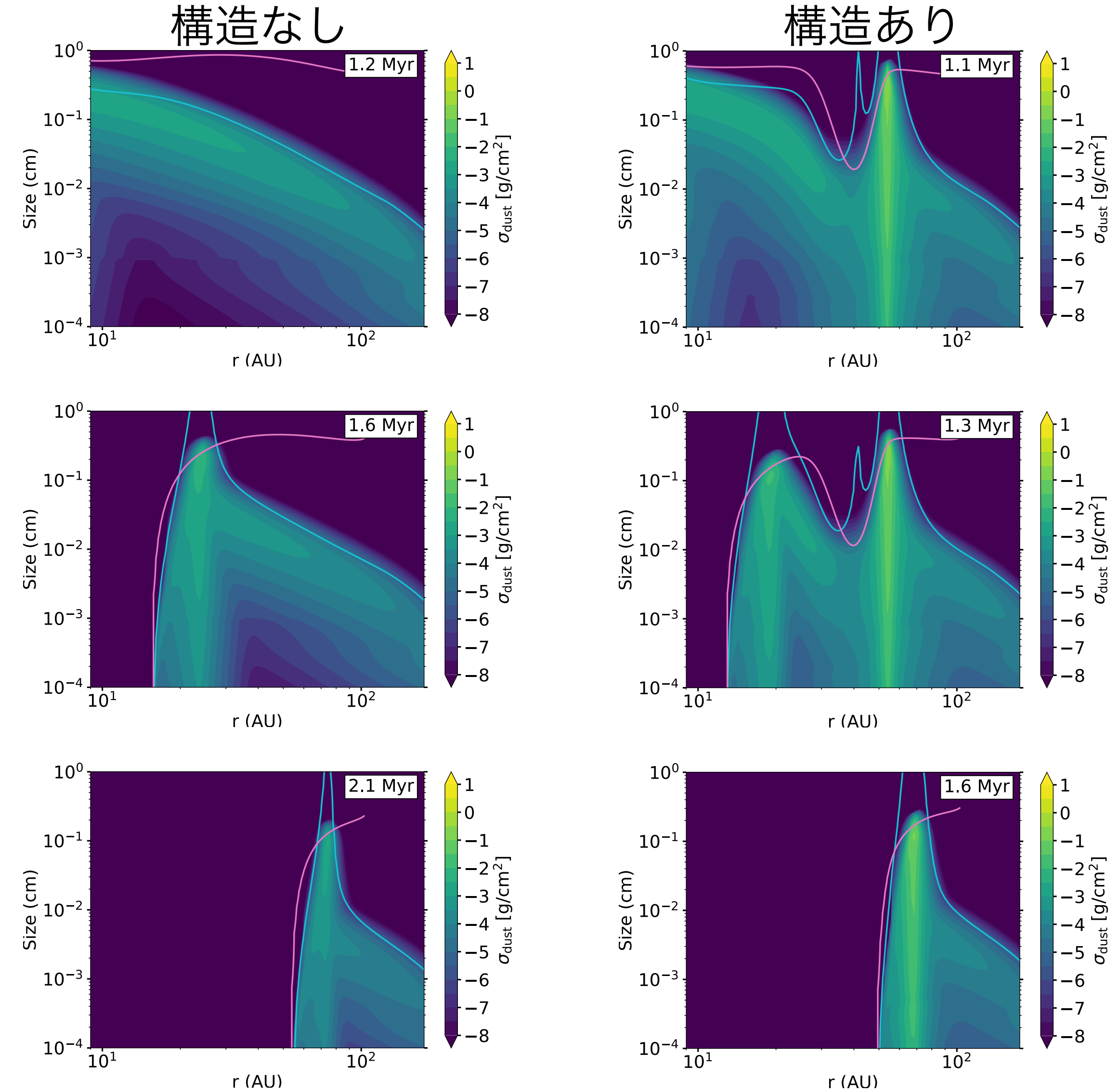


Fig. 4. Dust size distribution for a smooth disk at 1.2, 1.6, and 2.1 Myr. The drift (cyan) and fragmentation (pink) growth limits are also indicated.

Fig. 5. Dust size distribution for a structured disk at 1.1, 1.3, and 1.6 Myr. The drift (cyan) and fragmentation (pink) growth limits are also indicated. The last two snapshots were selected to match the ones of Figure 4 in terms of the photoevaporative cavity size.

Millimeter emission in photoevaporating disks is determined by early substructures (Gárate et al. 2023)

結果

- ミリ波フラックス

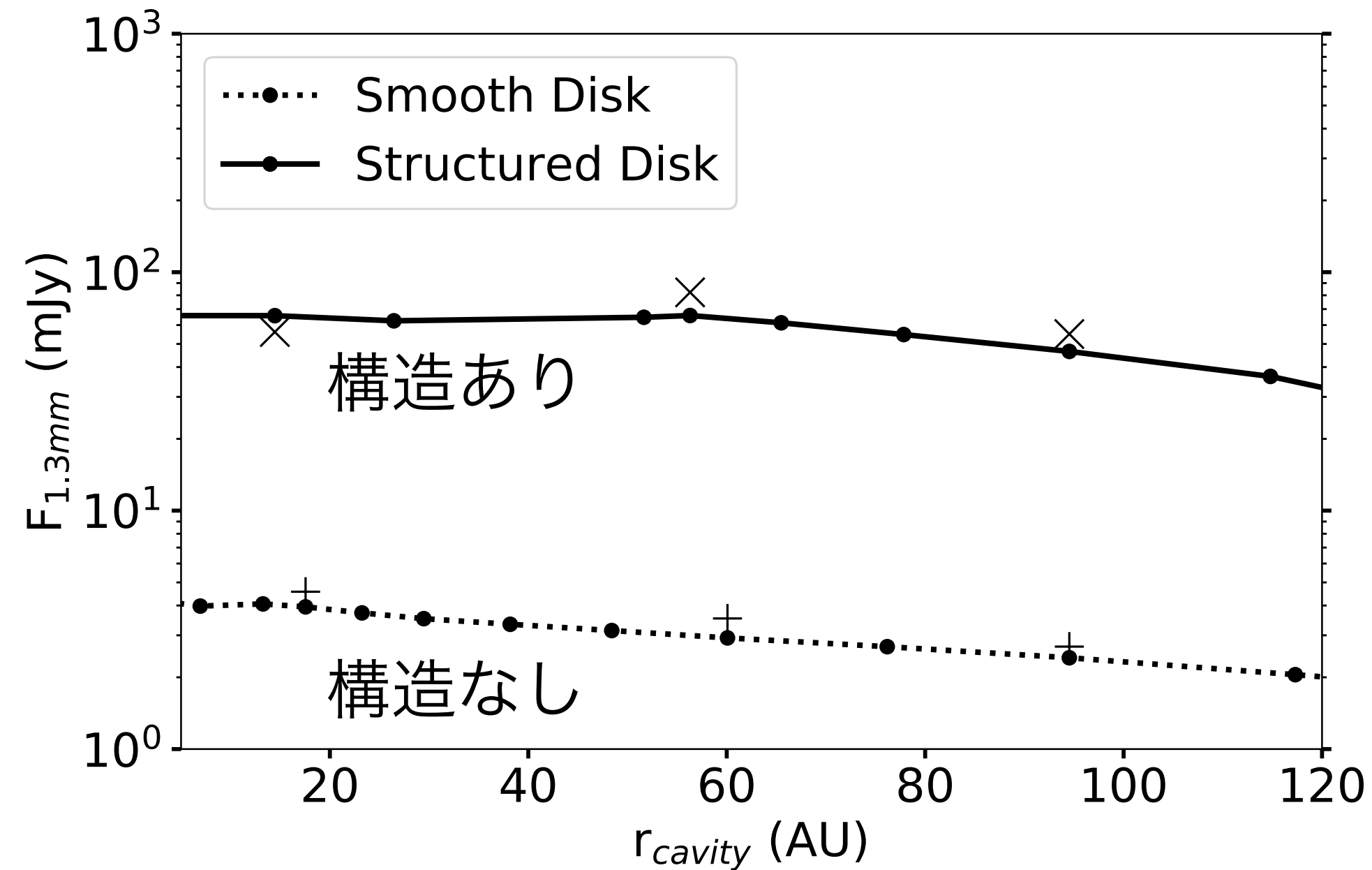


Fig. 6. Millimeter fluxes F_{mm} , as a function of the size of the photoevaporative cavity for the smooth (dotted) and structured (solid) disk models. The solid and dotted lines represent flux from the optically thin approximation (Equation 15). The markers are the fluxes obtained with RADMC-3D (“+” for the smooth disk, “x” for the structured disk). The disks are assumed to be at 140 pc, and no inclination. The cavity size measurement is based on the dust distribution of millimeter sized grains.

- 構造のあり/なしはSEDには影響をあまり与えない。

- X-ray光度の影響:
光度が高いと光蒸発cavityが開くのが早い。

→ 構造なしの場合、
cavityが開いたときの
ダスト質量と
ミリ波フラックスが
より高くなる。

→ 構造ありの場合、
X-ray光度に
あまり依存しない。

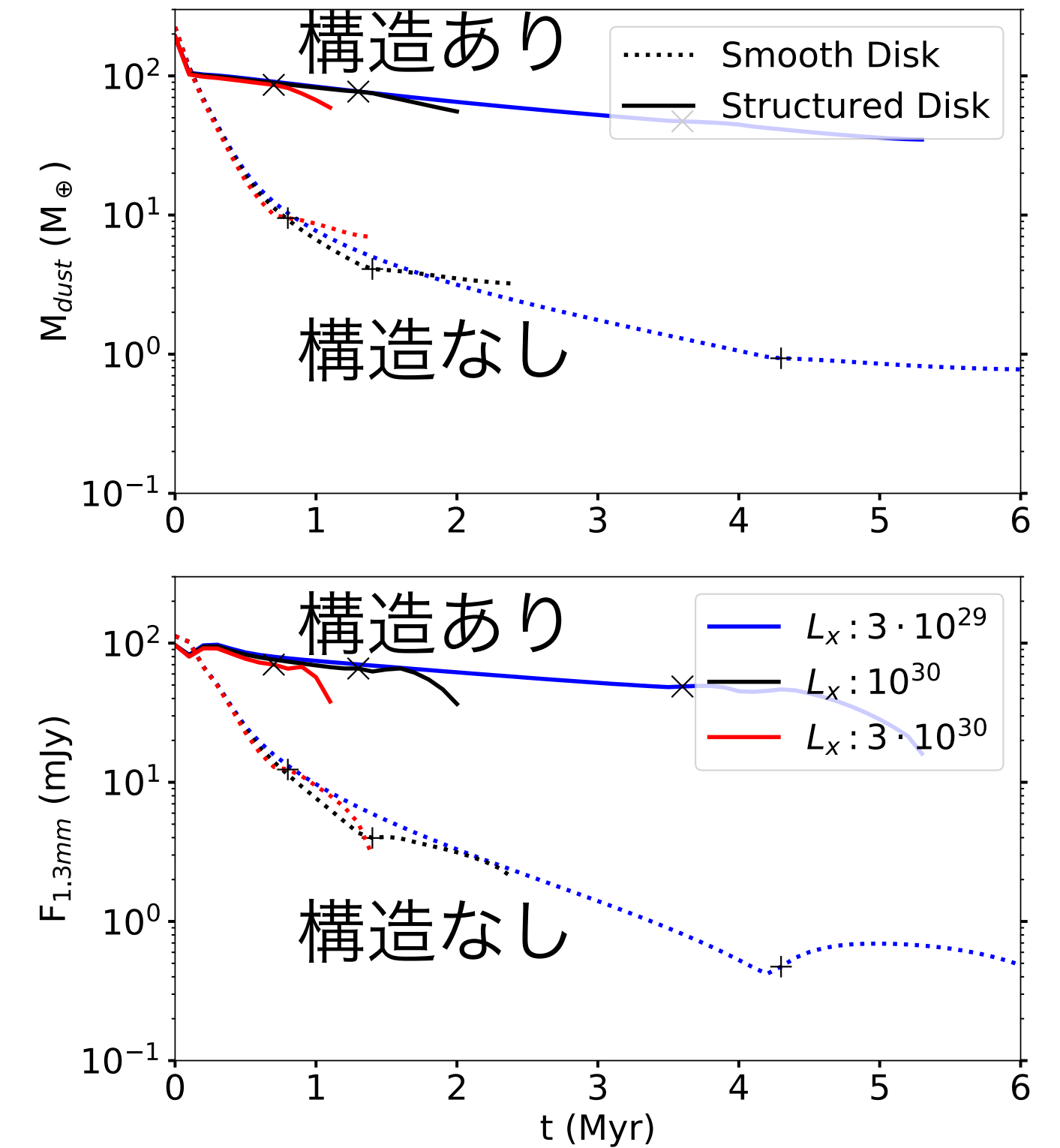


Fig. 8. Evolution of the dust mass (top) and disk flux at $\lambda = 1.3$ mm (bottom, assuming a distance of 140 pc), for different X-ray luminosities L_x , with the black line corresponding to the fiducial value. The markers indicate the moment when photoevaporation opens a cavity in the inner disk (“+” for the smooth disk, “x” for the structured disk).

Millimeter emission in photoevaporating disks is determined by early substructures (Gárate et al. 2023)

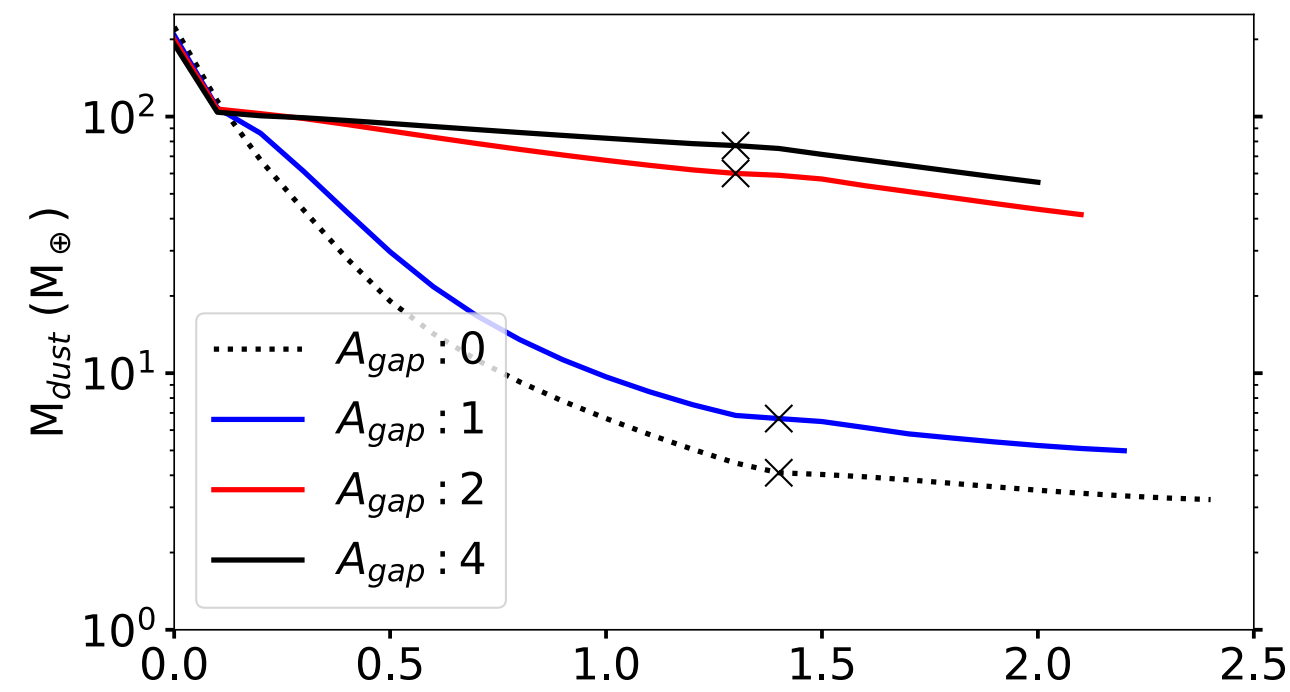
結果

- 構造ありの場合のギャップ深さ依存性

乱流強度:

$$\alpha(r) = \alpha_0 \times \left(1 + A_{\text{gap}} \exp \left(-\frac{(r - r_{\text{gap}})^2}{2w_{\text{gap}}^2} \right) \right),$$

- ギャップ位置 r_{gap} は結果にあまり影響を与えない。
- オパシティモデルを変えても傾向は変わらない。



$A_{\text{gap}} = 2$
→ 土星質量相当

$A_{\text{gap}} = 1, 2$ の
間に境界

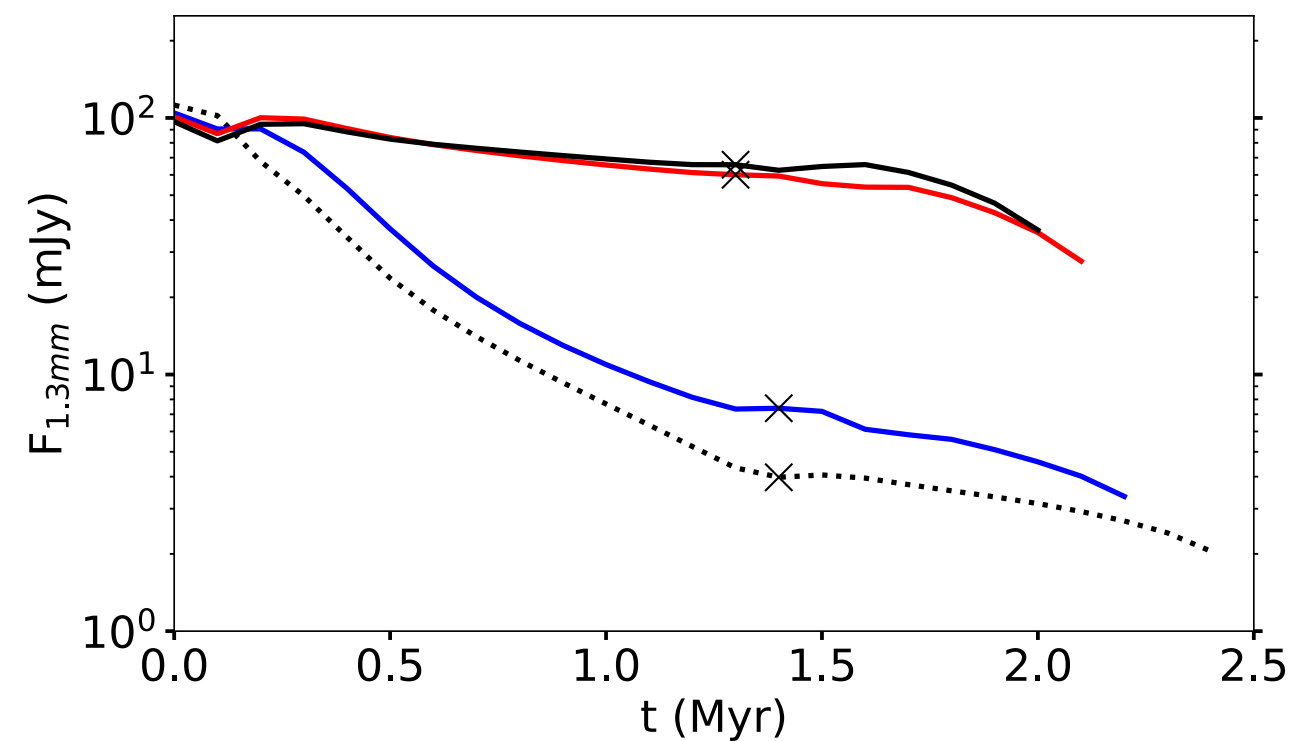


Fig. 9. Same as Figure 8, but for structured disks with different gap amplitudes, with a fixed location at $r_{\text{gap}} = 40$ AU and X-ray luminosity of $L_x = 10^{30} \text{ erg s}^{-1}$. Notice that the axis scales are different from Figure 8.

Millimeter emission in photoevaporating disks is determined by early substructures (Gárate et al. 2023)

議論

- 光蒸発: ガストダストに深いcavityを作る。深いcavityには惑星の存在は関係ない。
早期のsubstructuresの有無: 円盤のミリ波フラックスを決める。明るい遷移円盤は土星質量の惑星で説明できる。
- 遷移円盤の比較的高い降着率: 内側領域にデッドゾーンがあれば、内側円盤が長期に渡って残り、光蒸発でcavityが開いたとしても高い降着率を説明できる。
- substructuresと光蒸発cavityが両方ある場合の進化: 2つのリングが1つに合体する。合体したあとは光蒸発でリング位置が決まるので、substructuresを作っていた惑星に関する情報をリングから得ることはできなくなる。

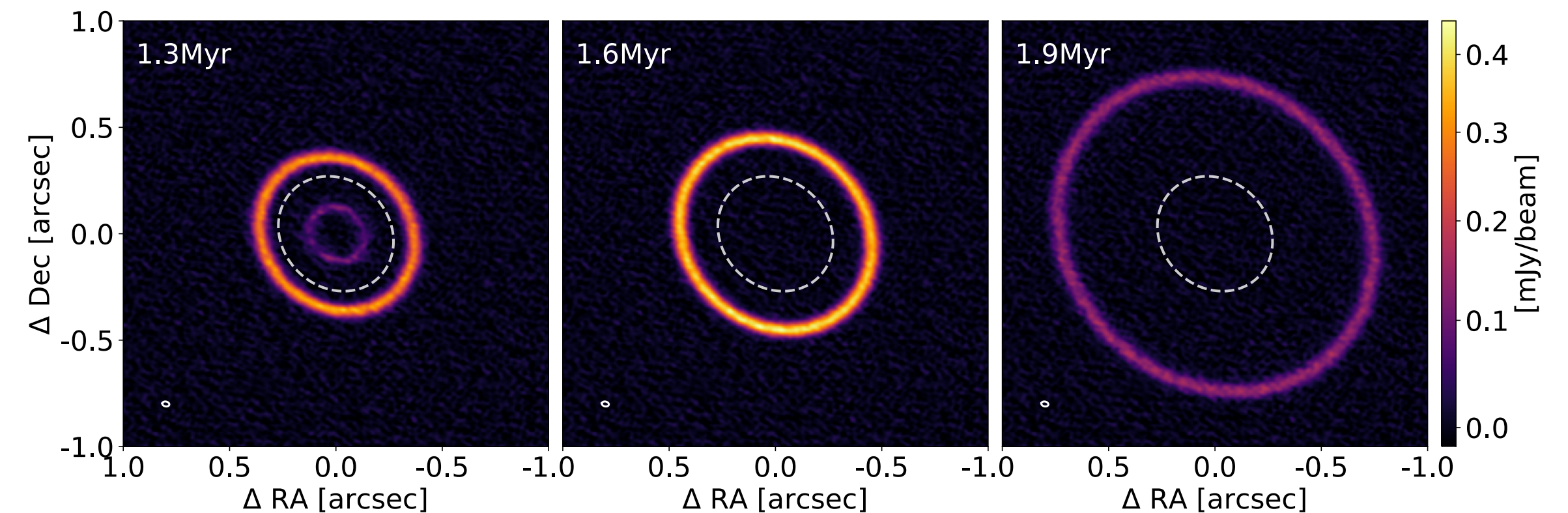


Fig. 11. Synthetic ALMA observations at 1.3 mm of the structured disk model at 1.3 Myr, 1.6 Myr, and 1.8 Myr, generated using the SIMIO package (Kurtovic et al., in prep.) to post-process our radiative transfer model. The image shows how our disk would look if it was observed with the same ALMA configuration of Elias24 (Huang et al. 2018, from the DSHARP sample), assuming a distance of 139 pc and an inclination of 29°. The beam size is plotted in the lower-left corner. The orbit of the primordial gap ($r_{\text{gap}} = 40$ AU) is marked with a dashed line. We note that this is not intended to be a comparison “with” Elias24.

FAUST X: Formaldehyde in the Protobinary System [BHB2007] 11: Small Scale Deuteration

Lucy Evans, Charlotte Vastel, Francisco Fontani, Jaime Pineda, Izaskun Jiménez-Serra, Felipe Alves, Takeshi Sakai, Mathilde Bouvier, Paola Caselli, Cecilia Ceccarelli, Claire Chandler, Brian Svoboda, Luke Maud, Claudio Codella, Nami Sakai, Romane Le Gal, Ana López-Sepulcre, George Moellenbrock, Satoshi Yamamoto ★

Context. Deuterium in H-bearing species is enhanced during the early stages of star formation, however, only a small number of high spatial resolution deuteration studies exist towards protostellar objects, leaving the small-scale structures unrevealed and understudied. Aims. We aim to constrain the deuterium fractionation ratios in a Class 0/I protostellar object in formaldehyde (H₂CO), which has abundant deuterated isotopologues in this environment. Methods. We observed the Class 0/I protobinary system [BHB2007] 11, whose emission components are embedded in circumstellar disks that have radii of 2-3 au, using ALMA within the context of the Large Program FAUST. The system is surrounded by a complex filamentary structure connecting to the larger circumbinary disk. In this work we present the first study of formaldehyde D-fractionation towards this source with detections of H₂CO 3(0,3)-2(0,2), combined with HDCO 4(2,2)-3(2,1), HDCO 4(1,4)-3(1,3) and D₂CO 4(0,4)-3(0,3). These observations enable multiple velocity components associated with the methanol hotspots also uncovered by FAUST data, as well as the external envelope, to be resolved. In addition, based on the kinematics seen in the observations of the H₂CO emission, we propose the presence of a second large scale outflow. Results. HDCO and D₂CO are only found in the central regions of the core while H₂CO is found more ubiquitously. From radiative transfer modelling, the column densities ranges found for H₂CO, HDCO and D₂CO are $(3-8) \times 10^{14} \text{ cm}^{-2}$, $(0.8-2.9) \times 10^{13} \text{ cm}^{-2}$ and $(2.6-4.3) \times 10^{12} \text{ cm}^{-2}$, respectively, yielding an average D/H ratio of 0.01-0.04. Following the results of kinematic modelling, the second large scale feature is inconsistent with a streamer-like nature and we thus tentatively conclude that the feature is an asymmetric molecular outflow launched by a wide-angle disk wind.

Evolution of Chemistry in the envelope of Hot Corinos (ECHOS). I. Extremely young sulphur chemistry in the isolated Class 0 object B335

G. Esplugues, M. Rodríguez-Baras, D. San Andrés, D. Navarro-Almaida, A. Fuente, P. Rivière-Marichalar, Á. Sánchez-Monge, M. N. Drozdovskaya, S. Spezzano, P. Caselli ★ Within the project Evolution of Chemistry in the envelope of HOt corinoS (ECHOS), we present a study of sulphur chemistry in the envelope of the Class 0 source B335 through observations in the spectral range 7, 3, and 2 mm. We have modelled observations assuming LTE and LVG approximation. We have also used the code Nautilus to study the time evolution of sulphur species. We have detected 20 sulphur species with a total gas-phase S abundance similar to that found in the envelopes of other Class 0 objects, but with significant differences in the abundances between sulphur carbon chains and sulphur molecules containing oxygen and nitrogen. Our results highlight the nature of B335 as a source especially rich in sulphur carbon chains unlike other Class 0 sources. The low presence or absence of some molecules, such as SO and SO⁺, suggests a chemistry not particularly influenced by shocks. We, however, detect a large presence of HCS⁺ that, together with the low rotational temperatures obtained for all the S species (<15 K), reveals the moderate or low density of the envelope of B335. We also find that observations are better reproduced by models with a sulphur depletion factor of 10 with respect to the sulphur cosmic elemental abundance. The comparison between our model and observational results for B335 reveals an age of $10^4 < t < 10^5$ yr, which highlights the particularly early evolutionary stage of this source. B335 presents a different chemistry compared to other young protostars that have formed in dense molecular clouds, which could be the result of accretion of surrounding material from the diffuse cloud onto the protostellar envelope of B335. In addition, the analysis of the SO₂/C₂S, SO/CS, and HCS⁺/CS ratios within a sample of prestellar cores and Class 0 objects show that they could be used as good chemical evolutionary indicators of the prestellar to protostellar transition.

Millimetre and submillimetre spectroscopy of isobutene and its detection in the molecular cloud G+0.693

Mariyam Fatima, Holger S. P. Müller, Oliver Zingsheim, Frank Lewen, Víctor M. Rivilla, Izaskun Jiménez-Serra, Jesús Martín-Pintado, Stephan Schlemmer ★ Isobutene ($(\text{CH}_3)_2\text{C}=\text{CH}_2$) is one of the four isomers of butene (C_4H_8). Given the detection of propene ($\text{CH}_3\text{CH}=\text{CH}_2$) toward TMC-1, and also in the warmer environment of the solar-type protostellar system IRAS 16293–2422, one of the next alkenes, isobutene, is a promising candidate to be searched for in space. We aim to extend the limited line lists of the main isotopologue of isobutene from the microwave to the millimetre region in order to obtain a highly precise set of rest frequencies and to facilitate its detection in the interstellar medium. We investigated the rotational spectrum of isobutene in the 35–370 GHz range using absorption spectroscopy at room temperature. Quantum-chemical calculations were carried out to evaluate vibrational frequencies. We determined new or improved spectroscopic parameters for isobutene up to a sixth-order distortion constant. These new results enabled its detection in the G+0.693 molecular cloud for the first time, where propene was also recently found. The propene to isobutene column density ratio was determined to be about 3:1. The observed spectroscopic parameters for isobutene are sufficiently accurate that calculated transition frequencies should be reliable up to 700 GHz. This will further help in observing this alkene in other, warmer regions of the ISM.

A global view on star formation: The GLOSTAR Galactic plane survey VIII. Formaldehyde absorption in Cygnus X

Y. Gong, G. N. Ortiz-León, M. R. Rugel, K. M. Menten, A. Brunthaler, F. Wyrowski, C. Henkel, H. Beuther, S. A. Dzib, J. S. Urquhart, A. Y. Yang, J. D. Pandian, R. Dokara, V. S. Veena, H. Nguyen, S. -N. X. Medina, W. D. Cotton, W. Reich, B. Winkel, P. Müller, I. Skretas, T. Csengeri, S. Khan, A. Cheema ★ Cygnus X is one of the closest and most active high-mass star-forming regions in our Galaxy, making it one of the best laboratories for studying massive star formation. As part of the GLOSTAR Galactic plane survey, we performed large scale simultaneous H₂CO (1_{1,0}-1_{1,1}) spectral line and radio continuum imaging observations toward Cygnus X at $\lambda \sim 6$ cm with the Karl G. Jansky Very Large Array and the Effelsberg-100 m radio telescope. Our Effelsberg observations reveal widespread H₂CO (1_{1,0}-1_{1,1}) absorption with a spatial extent of $\gtrsim 50$ pc in Cygnus X for the first time. On large scales of 4.4 pc, the relative orientation between local velocity gradient and magnetic field tends to be more parallel at H₂ column densities of $\gtrsim 1.8 \times 10^{22}$ cm⁻². On the smaller scale of 0.17 pc, our VLA+Effelsberg combined data reveal H₂CO absorption only toward three bright HII regions. Our observations demonstrate that H₂CO (1_{1,0}-1_{1,1}) is commonly optically thin. Kinematic analysis supports the assertion that molecular clouds generally exhibit supersonic motions on scales of 0.17-4.4 pc. We show a non-negligible contribution of the cosmic microwave background radiation in producing extended absorption features in Cygnus X. Our observations suggest that H₂CO (1_{1,0} – 1_{1,1}) can trace molecular gas with H₂ column densities of $\gtrsim 5 \times 10^{21}$ cm⁻². The ortho-H₂CO fractional abundance with respect to H₂ has a mean value of 7.0×10^{-10} . A comparison of velocity dispersions on different linear scales suggests that the dominant -3 km s⁻¹ velocity component in the prominent DR21 region has nearly identical velocity dispersions on scales of 0.17-4.4 pc, which deviates from the expected behavior of classic turbulence.

Protonated hydrogen cyanide as a tracer of pristine molecular gas

Y. Gong, F. J. Du, C. Henkel, A. M. Jacob, A. Belloche, J. Z. Wang, K. M. Menten, W. Yang, D. H. Quan, C. T. Bop, G. N. Ortiz-León, X. D. Tang, M. R. Rugel, S. Liu ★ Protonated hydrogen cyanide, HCNH^+ , plays a fundamental role in astrochemistry because it is an intermediary in gas-phase ion-neutral reactions within cold molecular clouds. However, the impact of the environment on the chemistry of HCNH^+ remains poorly understood. With the IRAM-30 m and APEX-12 m observations, we report the first robust distribution of HCNH^+ in the Serpens filament and in Serpens South. Our data suggest that HCNH^+ is abundant in cold and quiescent regions, but is deficit in active star-forming regions. The observed HCNH^+ fractional abundances relative to H_2 range from 3.1×10^{-11} in protostellar cores to 5.9×10^{-10} in prestellar cores, and the HCNH^+ abundance generally decreases with increasing H_2 column density, which suggests that HCNH^+ coevolves with cloud cores. Our observations and modeling results suggest that the abundance of HCNH^+ in cold molecular clouds is strongly dependent on the H_2 number density. The decrease in the abundance of HCNH^+ is caused by the fact that its main precursors (e.g., HCN and HNC) undergo freeze-out as the number density of H_2 increases. However, current chemical models cannot explain other observed trends, such as the fact that the abundance of HCNH^+ shows an anti-correlation with that of HCN and HNC, but a positive correlation with that of N_2H^+ in the southern part of the Serpens South northern clump. This indicates that additional chemical pathways have to be invoked for the formation of HCNH^+ via molecules like N_2 in regions in which HCN and HNC freeze out. Both the fact that HCNH^+ is most abundant in molecular cores prior to gravitational collapse and the fact that low- J HCNH^+ transitions have very low H_2 critical densities make this molecular ion an excellent probe of pristine molecular gas.

JOYS: Disentangling the warm and cold material in the high-mass IRAS 23385+6053 cluster

C. Gieser, H. Beuther, E. F. van Dishoeck, L. Francis, M. L. van Gelder, L. Tychoniec, P. J. Kavanagh, G. Perotti, A. Caratti o Garatti, T. P. Ray, P. Klaassen, K. Justtanont, H. Linnartz, W. R. M. Rocha, K. Slavicinska, L. Colina, M. Güdel, Th. Henning, P. -O. Lagage, G. Östlin, B. Vandenbussche, C. Waelkens, G. Wright ★ (abridged) We study and compare the warm (>100 K) and cold (<100 K) material toward the high-mass star-forming region IRAS 23385+6053 (IRAS 23385 hereafter) combining high angular resolution observations in the mid-infrared (MIR) with the JWST Observations of Young protoStars (JOYS) project and with the NOEMA at mm wavelengths at angular resolutions of 0.2"-1". The spatial morphology of atomic and molecular species is investigated by line integrated intensity maps. The temperature and column density of different gas components is estimated using H₂ transitions (warm and hot component) and a series of CH₃CN transitions as well as 3 mm continuum emission (cold component). Toward the central dense core in IRAS 23385 the material consists of relatively cold gas and dust (~ 50 K), while multiple outflows create heated and/or shocked H₂ and show enhanced temperatures (~ 400 K) along the outflow structures. An energetic outflow with enhanced emission knots of [Fe II] and [Ni II] hints at J-type shocks, while two other outflows have enhanced emission of only H₂ and [S I] caused by C-type shocks. The latter two outflows are also more prominent in molecular line emission at mm wavelengths (e.g., SiO, SO, H₂CO, and CH₃OH). Even higher angular resolution data are needed to unambiguously identify the outflow driving sources given the clustered nature of IRAS 23385. While most of the forbidden fine structure transitions are blueshifted, [Ne II] and [Ne III] peak at the source velocity toward the MIR source A/mmA2 suggesting that the emission is originating from closer to

Delivery of icy planetesimals to inner planets in the Proxima Centauri planetary system

S. I. Ipatov ★ The estimates of the delivery of icy planetesimals from the feeding zone of Proxima Centauri c (with mass equal to $7m_E$, m_E is the mass of the Earth) to inner planets b and d were made. They included the studies of the total mass of planetesimals in the feeding zone of planet c and the probabilities of collisions of such planetesimals with inner planets. This total mass could be about $10\text{--}15m_E$. It was estimated based on studies of the ratio of the mass of planetesimals ejected into hyperbolic orbits to the mass of planetesimals collided with forming planet c. At integration of the motion of planetesimals, the gravitational influence of planets c and b and the star was taken into account. In most series of calculations, planetesimals collided with planets were excluded from integrations. Based on estimates of the mass of planetesimals ejected into hyperbolic orbits, it was concluded that during the growth of the mass of planet c the semi-major axis of its orbit could decrease by at least a factor of 1.5. Depending on possible gravitational scattering due to mutual encounters of planetesimals, the total mass of material delivered by planetesimals from the feeding zone of planet c to planet b was estimated to be between $0.002m_E$ and $0.015m_E$. Probably, the amount of water delivered to Proxima Centauri b exceeded the mass of water in Earth's oceans. The amount of material delivered to planet d could be a little less than that delivered to planet b.

The Global Structure of Molecular Clouds: I. Trends with Mass and Star Formation Rate

Nia Imara, John C. Forbes ★ We introduce a model for the large-scale, global 3D structure of molecular clouds. Motivated by the morphological appearance of clouds in surface density maps, we model clouds as cylinders, with the aim of backing out information about the volume density distribution of gas and its relationship to star formation. We test our model by applying it to surface density maps for a sample of nearby clouds and find solutions that fit each of the observed radial surface density profiles remarkably well. Our most salient findings are that clouds with higher central volume densities are more compact and also have lower total mass. These same lower-mass clouds tend to have shorter gas depletion times, regardless of whether we consider their total mass or dense mass. Our analyses lead us to conclude that cylindrical clouds can be characterized by a universal structure that sets the timescale on which they form stars.

The population of young low-mass stars in Trumpler 14

Dominika Itrich, Leonardo Testi, Giacomo Beccari, Carlo F. Manara, Megan Reiter, Thomas Preibisch, Anna F. McLeod, Giovanni Rosotti, Ralf Klessen, Sergio Molinari, Patrick Hennebelle ★ Massive star-forming regions are thought to be the most common birth environments in the Galaxy and the only birth places of very massive stars. Their presence in the stellar cluster alters the conditions within the cluster impacting at the same time the evolution of other cluster members. In principle, copious amounts of ultraviolet radiation produced by massive stars can remove material from outer parts of the protoplanetary disks around low- and intermediate-mass stars in the process of external photoevaporation, effectively reducing the planet-formation capabilities of those disks. Here, we present deep VLT/MUSE observations of low-mass stars in Trumpler 14, one of the most massive, young, and compact clusters in the Carina Nebula Complex. We provide spectral and stellar properties of 717 sources and based on the distribution of stellar ages derive the cluster age of ~ 1 Myr. The majority of the stars in our sample have masses $\leq 1 M_{\odot}$, what makes our spectroscopic catalogue the most deep to date in term of masses, and proves that detailed investigations of low-mass stars are possible in the massive but distant regions. Spectroscopic studies of low-mass members of the whole Carina Nebula Complex are missing. Our work provides an important step forward towards filling this gap and set the stage for follow-up investigation of accretion properties in Trumpler 14.

Rotational Variability and Detection of Superflares in a Young Brown Dwarf by TESS

Rajib Kumbhakar, Soumen Mondal, Samrat Ghosh, Diya Ram, Sudip Pramanik ★ We present a comprehensive analysis of a Transiting Exoplanet Survey Satellite (TESS) high-quality light curve for a young brown dwarf, MHO 4 having spectral type M7.0, in the Taurus star-forming region. We investigate the rotation periods and characterize the BD's dynamic atmosphere and surface features. We present light curve analysis of MHO 4, and estimate the rotation period to be around 2.224 d. Remarkably, MHO 4 exhibits two significant flaring events. Furthermore, we also estimated bolometric flare energies to be within the energy range of 10^{34} to 10^{35} erg, which sits in the superflare category.

SOFIA FEEDBACK Survey: The Pillars of Creation in [C II] and Molecular Lines

Ramsey L. Karim, Marc W. Pound, Alexander G. G. M. Tielens, Maitraiye Tiwari, Lars Bonne, Mark G. Wolfire, Nicola Schneider, Ümit Kavak, Lee G. Mundy, Robert Simon, Rolf Güsten, Jürgen Stutzki, Friedrich Wyrowski, Netty Honingh ★ We investigate the physical structure and conditions of photodissociation regions (PDRs) and molecular gas within the Pillars of Creation in the Eagle Nebula using SOFIA FEEDBACK observations of the [C II] 158 micron line. These observations are velocity resolved to 0.5 km s^{-1} and are analyzed alongside a collection of complimentary data with similar spatial and spectral resolution: the [O I] 63 micron line, also observed with SOFIA, and rotational lines of CO, HCN, HCO^+ , CS, and N_2H^+ . Using the superb spectral resolution of SOFIA, APEX, CARMA, and BIMA, we reveal the relationships between the warm PDR and cool molecular gas layers in context of the Pillars' kinematic structure. We assemble a geometric picture of the Pillars and their surroundings informed by illumination patterns and kinematic relationships and derive physical conditions in the PDRs associated with the Pillars. We estimate an average molecular gas density $n_{\text{H}_2} \sim 1.3 \times 10^5 \text{ cm}^{-3}$ and an average atomic gas density $n_{\text{H}} \sim 1.8 \times 10^4 \text{ cm}^{-3}$ and infer that the ionized, atomic, and molecular phases are in pressure equilibrium if the atomic gas is magnetically supported. We find pillar masses of 103, 78, 103, and 18 solar masses for P1a, P1b, P2, and P3 respectively, and evaporation times of $\sim 1\text{-}2 \text{ Myr}$. The dense clumps at the tops of the pillars are currently supported by the magnetic field. Our analysis suggests that ambipolar diffusion is rapid and these clumps are likely to collapse within their photoevaporation timescales.

A resolved rotating disk wind from a young T Tauri star in the Bok globule CB26

R. Launhardt, Ya. N. Pavlyuchenkov, V. V. Akimkin, A. Dutrey, F. Gueth, S. Guilloteau, Th. Henning, V. Pietu, K. Schreyer, D. Semenov, B. Stecklum, T. L. Bourke ★ The disk-outflow connection plays a key role in extracting excess angular momentum from a forming protostar. We have previously reported the discovery of a small molecular outflow from the edge-on T Tauri star in the Bok globule CB26 that shows a peculiar velocity pattern, reminiscent of an outflow that corotates with the disk. We report new, high-resolution mm-interferometric observations of CB26 with the aim of revealing the morphology and kinematics of the outflow at the disk-outflow interface. The IRAM PdBI was used to observe CO(2-1) at 1.3mm with a resolution of 0.5". Using a physical model of the disk, which was derived from the dust emission, we employed chemo-dynamical modeling combined with line radiative transfer to constrain kinematic parameters and to construct a model of the CO emission from the disk that allowed us to separate the emission of the disk from that of the outflow. Our observations confirm the disk-wind nature of the rotating molecular outflow from CB26. The new high-resolution data reveal an X-shaped morphology of the CO emission close to the disk, and vertical streaks extending from the disk surface with a small half-opening angle of 7° , which can be traced out to vertical heights of 500au. We interpret this emission as the combination of the disk atmosphere and a well-collimated disk wind, which we trace down to vertical heights of 40au, where it is launched from the surface of the flared disk at radii of 20-45au. The observed CO outflow has a total momentum flux of $1e-5$ Msun km/s/yr, which is nearly three orders of magnitude larger than the maximum thrust that can be provided by the luminosity of the central star. We conclude that photoevaporation cannot be the main driving mechanism for this outflow, but it must be predominantly an MHD disk wind. It is thus far the best-resolved rotating disk wind observed to be launched from a circumstellar disk.